

1 Ammonia emission estimates using CrIS satellite observations over 2 Europe

3 Jieying Ding^{1*}, Ronald van der A¹, Henk Eskes¹, Enrico Damers², Mark Shephard³, Roy
4 Wichink Kruit⁴, Marc Guevara⁵, Leonor Tarrason⁶

5 1. Royal Netherlands Meteorological Institute (KNMI), De Bilt, The Netherlands

6 2. Netherlands Organisation for Applied Scientific Research (TNO), Utrecht, The Netherlands

7 3. Environment and Climate Change Canada (ECCC), Toronto, Ontario, Canada

8 4. National Institute for Public Health and the Environment, Bilthoven, The Netherlands

9 5. Barcelona Supercomputing Center, Barcelona, Spain

10 6. NILU – Norwegian Institute for Air Research, Kjeller, Norway

11

12 *Corresponding authors: Jieying Ding (jieying.ding@knmi.nl)

13

14

15 Abstract

16

17 Over the past century ammonia (NH₃) emissions have increased with the growth of livestock and
18 fertilizer usage. The abundant NH₃ emissions lead to secondary fine particulate matter (PM_{2.5}) pollution,
19 climate change, reduction in biodiversity and affect human health. Up-to-date and spatially and
20 temporally resolved information of NH₃ emissions is essential to better quantify its impact. In this study
21 we applied the existing DECSO (Daily Emissions Constrained by Satellite Observations) algorithm to
22 NH₃ observations from the Cross-track Infrared Sounder (CrIS) to estimate NH₃ emissions. Because
23 NH₃ in the atmosphere is influenced by Nitrogen Oxides (NO_x), we implemented DECSO to estimate
24 NO_x and NH₃ emissions simultaneously. The emissions are derived over Europe for 2020 on a spatial
25 resolution of 0.2° × 0.2° using daily observations from both CrIS and TROPOMI (on the Sentinel 5p
26 satellite). Due to the limited number of daily satellite observations of NH₃, monthly emissions of NH₃
27 are reported. The total NH₃ emissions derived from observations are about 8 Tg/year with a precision
28 of about 5-17 % per grid cell per year over the European domain [-10° ~30° E, 35° ~ 55° N]. The
29 comparison of the satellite-derived NH₃ emissions from DECSO with independent bottom-up
30 inventories and in-situ observations indicates a consistency in terms of magnitude on the country totals,

31 the results also being comparable regarding the temporal and spatial distributions. The validation of
32 DECSO over Europe implies that we can use DECSO to quickly derive fairly good monthly emissions
33 of NH₃ over regions with limited local information of NH₃ emissions.

34

35

36 1 Introduction

37

38 Ammonia (NH₃) is the most abundant alkaline gas and one of the main reactive nitrogen species in the
39 atmosphere. NH₃ is a precursor for the formation of atmospheric aerosols, which play an important role
40 in climate change. In Europe, about 50% (Wyer et al., 2022) of atmospheric NH₃ is transformed into
41 fine particulate matter (PM_{2.5}) composed of ammonium through chemical reactions with sulfuric and
42 nitric acids from nitrogen oxides (NO_x) and sulphur dioxides (SO₂) in the atmosphere (Renard et al.,
43 2004; Schaap et al., 2004). According to the European Environment Agency (EEA), the dominant
44 source of NH₃ in Europe is agriculture, which was responsible for more than 90% of the European
45 emissions. The other source sectors include industry, transport, energy, waste treatment and biomass
46 burning (Behera et al., 2013; Backes et al., 2016a; Van Damme et al., 2018; Adams et al., 2019).
47 Excessive NH₃ emissions have adverse impact on biodiversity, human health, and climate change
48 (Galloway et al., 2008). Over the past century, NH₃ emissions increased strongly with the growing
49 human population, cattle farming and fertilizer usage (Crippa et al., 2023; Erisman et al., 2008; Van
50 Damme et al., 2021), leading to high nitrogen deposition loads to water and soil (Erisman et al., 2013)
51 with the associated eutrophication, acidification and biodiversity loss problems (Behera et al., 2013).
52 Since 2019, the Dutch policy makers paid a lot of attention to NH₃ emissions due to the nitrogen (N)
53 crisis after the national programmatic approach to nitrogen was rejected by the supreme court, because
54 it was inadequate for the protection of vulnerable nature areas (named Natura 2000). The Dutch
55 government is obliged by EU laws to protect the natural environment and prevent damage caused by
56 too high emissions of reactive nitrogen. Studies show that abatement of NH₃ emissions is very cost-
57 effective to improve air quality and have high social benefits (Backes et al., 2016b; Zhang et al., 2020;
58 Gu et al., 2021). Detailed spatially and temporally resolved information of NH₃ emissions is crucial for
59 both scientific communities and policy makers to study and predict pollutant concentrations and
60 deposition with their impact on the environment and to motivate environmental control strategies.

61 The empirical method to estimate NH₃ emissions is the so-called bottom-up approach, which combines
62 available official reported activity data incorporating a full differentiation of emission activities with
63 emission factors, and technology and abatement measures from individual countries for each source
64 category (Crippa et al., 2018; Crippa et al., 2023; Janssens-Maenhout et al., 2019). The annual emissions

65 are then distributed in time and space based on proxy data such as land use data, and meteorological
66 parameters (Backes et al., 2016a). Ge et al. (2020) summarized the key factors of agricultural NH₃
67 emissions: local agricultural practices, manure and fertilizer application including type, amount and
68 method, animal species, housing, manure storage, meteorological conditions, soil properties, and
69 regulations of agricultural practice. The uncertainties of NH₃ emissions calculated by the bottom-up
70 approach are very large due to insufficient data on agricultural activities (Behera et al., 2013; Beusen
71 et al., 2008). Crippa et al. (2018) pointed out that the uncertainty of NH₃ (between 186 % and 294.4 %)
72 in the EDGAR (The Emissions Database for Global Atmospheric Research) inventory is the largest
73 among all pollutants because of the high uncertainty of both agricultural statistics and emission factors.

74 The validation of NH₃ emission inventories using ground-based observations is very challenging due
75 to the sparsely distributed in-site measurement network. NH₃ concentrations have large temporal and
76 spatial variability due to its short lifetime, which ranges from about a few hours to two days (Dammers
77 et al., 2019; Luo et al., 2022). Densely distributed hourly or daily ground measurements are impractical
78 for large areas due to high costs and specific operational requirements (Noordijk et al., 2020). In the
79 last decade, a wide spatial and temporal coverage of satellite observations of NH₃ in lower troposphere
80 was established due to the development of infrared nadir viewing satellite instruments, such as the
81 Tropospheric Emission Spectrometer (TES) (Beer et al., 2008) on the NASA Aura satellite. The
82 operational Cross-track Infrared Sounder (CrIS) (Shephard and Cady-Pereira, 2015) on the Suomi
83 National Polar-orbiting Partnership (S-NPP) and on the Joint Polar Satellite System-1 and System-2
84 (JPSS-1 and JPSS-2, also named as NOAA-20 and NOAA-21) satellites of NASA/NOAA, and the
85 Infrared Atmospheric Sounder Interferometer (IASI) (Clarisse et al., 2009) on the MetOp satellites from
86 the European Space Agency (ESA), with their large swaths, provide daily global coverage of NH₃
87 observations and improve our understanding of NH₃ global distribution and temporal variability.

88 NH₃ emissions can be obtained by applying an inversion algorithm to satellite observations. Such
89 estimates provide useful information which is independent from bottom-up inventories. By using IASI
90 NH₃ observations, Van Damme et al. (2018) identified NH₃ emission hotspots and calculated emissions
91 based on a mass balance approach. They found that NH₃ emissions of most hotspots, especially
92 industrial emitters, were largely underestimated compared to EDGAR. Dammers et al. (2019) used both
93 IASI and CrIS observations to derive emissions, lifetimes and plume widths of NH₃ from large
94 agricultural and industrial point sources and concluded that 55 locations were missing in the
95 Hemispheric Transport Atmospheric Pollution version 2 (HTAPv2) emission inventory. Besides the
96 studies on point sources, data assimilation techniques combining a chemical transport model (CTM)
97 with satellite observations are also widely used to derive NH₃ surface emissions. van der Graaf et al.
98 (2022) adjusted the NH₃ emissions over Europe using a local ensemble transport Kalman filter (LETKF)
99 applied to CrIS NH₃ profiles. Sitwell et al. (2022) developed an ensemble-variational inversion system
100 to estimate NH₃ emissions from CrIS over North America. Another widely used method is 4D-Var

101 using the GEOS-Chem global chemistry transport model, which has been applied to America, China
102 and Europe using NH₃ observation from different instruments (Zhu et al., 2013; Zhang et al., 2018; Li
103 et al., 2019; Cao et al., 2020; Chen et al., 2021; Cao et al., 2022). The main advantage of CrIS is the
104 combination of global coverage and the improved sensitivity in the boundary layer attributed to the low
105 spectral noise of about 0.04 K at 280 K in the NH₃ spectral band (Zavalyov et al., 2013). The infrared
106 instrument is also more sensitive at the overpass time in the early afternoon with high thermal contrast
107 between air and surface.

108 The Daily Emissions Constrained by Satellite Observations (DECSO) inversion algorithm uses satellite
109 column observations to derive emissions for short-lived gases based on an extended Kalman Filter
110 (Mijling and van der A, 2012). The concentrations of the species are calculated from the emissions by
111 a CTM and compared to satellite observations. One of the main advantages to use DECSO is the fast
112 calculation speed compared to other data assimilation methods. Furthermore, the derived emissions are
113 updated by addition, not by scaling the existing emissions. This enables the fast detection of new sources
114 and changed emissions. In previous studies, DECSO has been applied to nitrogen dioxide (NO₂)
115 observations from different satellites and uses the Eulerian regional off-line CTM CHIMERE (Menut
116 et al., 2021; Menut et al., 2013) to estimate regional NO_x (NO₂+NO) emissions and it revealed that the
117 temporal and spatial variability of total surface NO_x emissions are well captured by DECSO compared
118 to bottom-up inventories or in-situ observations (Ding et al., 2015; Ding et al., 2017b; Ding et al., 2020;
119 van der A et al., 2020; Ding et al., 2022; Liu et al., 2018).

120 Direct validation of emission inventories, regardless of bottom-up or satellite-derived approaches,
121 presents the same challenge due to the inherent difficulty of directly measuring large-scale emissions
122 on the ground. The intercomparison of emissions using independent data and different approaches are
123 usually performed to assess the emission data. Another common way to validate emissions can be
124 achieved by using them as input data in a chemical transport model. The model simulated concentrations
125 are compared to in-situ observations.

126 In this study we extend the DECSO-NO_x system to NH₃ in order to derive both NO_x and NH₃ emissions
127 simultaneously, using CrIS NH₃ observations and NO₂ observations from the Tropospheric
128 Monitoring Instrument (TROPOMI) (Veefkind et al., 2012). Using the multi-species DECSO version,
129 we update NO_x and NH₃ emissions simultaneously to reduce the impact of the temporal change (e.g.
130 trend) of NO_x when deriving NH₃ emissions. After the description of the DECSO algorithm applied to
131 NH₃, the results of NH₃ emissions over Europe are presented at a spatial resolution of 0.2° × 0.2°. To
132 evaluate the derived NH₃ emissions, we will compare the country totals and the monthly variability
133 with bottom-up inventories with a focus on NH₃ emissions in the Netherlands. In addition, we compare
134 the NH₃ concentration simulations of CHIMERE using different emission inventories with in-situ
135 observations.

136

137 2 Data and Method

138 2.1 Satellite observations

139 2.1.1 CrIS observations of NH_3

140 The CrIS instrument is a Fourier transform spectrometer (FTS) launched on the Suomi National Polar-
141 orbiting Partnership (SNPP) satellite in 2011 and on the NOAA-20 satellite in 2017. The overpass time
142 of SNPP at the equator is about 01:30 and 13:30 local time. NOAA-20 circles the earth in the same orbit
143 as SNPP, but it is separated in time and space by 50 minutes and crosses the equator at about 02:20 and
144 14:20 local time. The instrument has a wide swath of up to 2200 km providing twice daily global
145 coverage. The total angular field-of-view consists of a 3×3 array of circular pixels of 14 km diameter
146 each at nadir (Han et al., 2013). CrIS measures the infrared spectrum including the main NH_3 spectral
147 signatures located in the longwave window region between 900 and 1000 cm^{-1} . The spectral resolution
148 of the radiance data is 0.625 cm^{-1} . NH_3 observations are retrieved with the CrIS Fast Physical Retrieval
149 (CFPR) algorithm based on an optimal estimate method minimizing the difference between measured
150 spectral radiances and those simulated by a radiative transfer model (Shephard and Cady-Pereira, 2015).
151 Three typical a priori profiles of NH_3 representing high-source, moderate-source and background source
152 are used in the retrieval algorithm. The NH_3 profiles are retrieved on 14 pressure levels with the peak
153 sensitivity of CrIS between 900 and 700 hPa (Shephard et al., 2020). For SNPP, the retrieval products
154 start from 2011 and ends in May 2021 with missing data from April to August in 2019. The NH_3 retrieval
155 product of NOAA-20 starts from March 2019. We use the version 1.6.4 retrieval products of CrIS on
156 both SNPP and NOAA-20 from September 2019 to December 2020, which also accounts for non-
157 detects in the observations and retrievals through optically thin clouds (White et al., 2023). We use the
158 daytime observations with the quality flag larger than 3 over our study domain of Europe [$-10^\circ \sim 30^\circ \text{E}$,
159 $35^\circ \sim 55^\circ \text{N}$] (Shephard et al., 2020). Since there are almost no emissions over ocean, we only use the
160 observations over land. To reduce extreme emission updates in one day we filter the NH_3 data larger
161 than the value at 99th percentile of all observations for the selected period over the study domain. This
162 has also been applied by van der Graaf et al. (2022). To make a fair comparison between NH_3
163 observations of CrIS and model simulations of CHIMERE, we interpolate modelled concentrations
164 from the model grid cell over the satellite footprints and apply the averaging kernel to the modelled
165 profile. Although the NH_3 observations from CrIS are in circular pixels, we still assume the pixel to be
166 rectangular and calculate the pixel corner coordinates based on the satellite height, satellite zenith angle
167 and viewing angle assuming the width of the pixel to be equal to the diameter of the circular pixel. To
168 simplify the calculation of applying the original logarithmic averaging kernels, we converted them to
169 linearized average kernels based on the method of Cao et al. (2022).

170

171 2.1.2 TROPOMI observations of NO₂

172 TROPOMI is onboard the Sentinel-5 Precursor (S5P) satellite launched on 13 October 2017 with the
173 high spatial resolution of $3.5 \times 5.5 \text{ km}^2$ at nadir for the NO₂ observations. The overpass time is about
174 13:30 local time, similar as for CrIS. We use TROPOMI tropospheric NO₂ columns from the version
175 2.4 reprocessed retrieval dataset (van Geffen et al., 2022) and follow the recommendations for using
176 the QA value as detailed in the Product User Manual (Eskes and Eichmann, 2022). NO₂ columns are
177 converted into ‘super-observations’ representing the integrated average (Boersma et al., 2016; Rijdsdijk
178 et al., 2024) over the $0.2^\circ \times 0.2^\circ$ grid cells. The super-observation error takes into account spatial
179 correlations between individual TROPOMI observations and representativity errors in the case of
180 incomplete coverage. In this paper, the super-observations are calculated for the NO₂ columns from
181 surface till about 700hPa where the NO₂ concentrations are most related to surface emissions. The
182 signal-to-noise ratio and calculation time of DECSO are improved by using super-observations. The
183 details of TROPOMI NO₂ data used by DECSO are described in Ding et al. (2020) and van der A et al.
184 (2024).

185

186 2.2 Ground-based observations.

187 To evaluate the NH₃ emissions derived by DECSO, we use independent ground-based observations in
188 2020 to compare with model simulated NH₃ concentrations of CHIMERE using different inventories.
189 Compared to other countries, Netherlands has the densest network for monitoring surface NH₃
190 concentrations. We use hourly NH₃ concentrations measured by mini-DOAS at six locations (Figure S1)
191 from the Dutch Monitoring Air Quality (LML) network (Berkhout et al., 2017) and monthly
192 measurements of NH₃ concentration provided by passive samples at 394 locations (Figure S2) from the
193 Dutch Measuring Ammonia in Nature (MAN) network (Lolkema et al., 2015). The uncertainty in NH₃
194 concentrations measured with individual passive samples is large (22% for a single monthly
195 measurement) and the measurements are calibrated monthly against the high-quality measurements
196 (about 20% for an hourly measurement) from the LML network to enhance the accuracy.

197

198 2.3 Emission inventories

199 To verify the satellite-derived emissions of NH₃ in Europe, we compare them to several emission
200 inventories including: the national emissions inventories officially reported under the Convention on
201 Long-range Transboundary Air Pollution (LRTAP) (Pinterits, 2023) of 2020, the emissions reported
202 under the European Pollutant Release and Transfer Register (E-PRTR) (EPTR, 2012) of 2020

203 including releases from industrial facilities and livestock facilities, the global emission inventory
 204 Hemispheric Transport of Air Pollution (HTAP) v3 of 2018 (Crippa et al., 2023), the Copernicus
 205 Atmosphere Monitoring Service (CAMS) Global anthropogenic emissions (CAMS-GLOB-ANT) v5.3
 206 of 2020 (Soulie et al., 2023), the regional European CAMS anthropogenic emission inventory (CAMS-
 207 REG-ANT) v5.1 of 2020 (Kuenen et al., 2022) and the Dutch official registered emissions of NH₃ in
 208 2020 (<https://data.emissieregistratie.nl/export>) (see Table 1). HTAP v3 has been developed by
 209 integrating official inventories over specific areas including CAMS-REG-ANT v5.1 for Europe with
 210 the EDGAR v6.1 inventory for the remaining world regions with the spatial resolution of 0.1° × 0.1°.
 211 CAMS-GLOB-ANT combines the EDGAR annual emissions and the Copernicus Atmosphere
 212 Monitoring Service TEMPOral profiles (CAMS-TEMPO) on a global scale (Guevara et al., 2021). The
 213 emissions of the most recent years are calculated based on the trends from the Community Emissions
 214 Data System (CEDS) global inventory (Hoesly et al., 2018). The resolution of CAMS-GLOB-ANT is
 215 0.1° × 0.1°. CAMS-REG-ANT v5.1 provide yearly emissions on the spatial resolution of 0.1° × 0.05°.
 216 We have applied the regional European CAMS-TEMPO profiles (Guevara et al., 2021) to CAMS-REG-
 217 ANT v5.1 to get the monthly emissions (hereinafter referred to as CAMS-REG-TEMPO). The Dutch
 218 registered NH₃ emissions are taken from <https://www.emissieregistratie.nl> and provided annually on a
 219 high resolution of 1 km × 1 km. To compare the derived NH₃ emissions of DECSO spatially with
 220 bottom-up inventories, we aggregate emissions from these bottom-up inventories into the 0.2° × 0.2°
 221 grid cells of the DECSO working domain.

222

223 *Table 1. Summary of the bottom-up inventories compared to the satellite-derived NH₃ emissions from DECSO.*

Emission inventory	Year	Spatial Resolution	Temporal resolution
LRTAP	2020	Country total	Annual
E-PRTR	2020	Point source	Annual
HTAP v3	2018	0.1° × 0.1°	Monthly
CAMS-GLOB-ANT v5.3	2020	0.1° × 0.1°	Monthly
CAMS-REG-ANT v5.1	2020	0.1° × 0.05°	Annual, monthly (with CAMS-REG-TEMPO)
Dutch Registered NH ₃ emissions	2020	1 km × 1 km	Annual

224

225 2.4 DECSO

226 DECSO is an inversion algorithm developed for the purpose of deriving emissions of short-lived species
227 from satellite observations. As such DECSO has been specifically designed to use daily satellite
228 observations of column concentrations to provide rapid updates of emission estimates of short-lived
229 atmospheric constituents on a regional scale. An extended Kalman filter is used, in which emissions are
230 translated to column concentrations via the CTM and these are compared to the satellite column
231 observations. Based on that single forward CTM simulation, the sensitivity of concentrations to
232 emissions is calculated by using trajectory analyses to account for transport away from the source. In
233 previous studies, DECSO has been applied to NO₂ observations from different satellites including
234 TROPOMI to estimate NO_x emissions (Mijling et al., 2013; Ding et al., 2015; van der A et al., 2020;
235 Ding et al., 2022; Ding et al., 2020; van der A et al., 2024). The studies revealed that the temporal and
236 spatial variability of total surface NO_x emissions are captured well by DECSO (Ding et al., 2017b; van
237 der A et al., 2017; Liu et al., 2018; van der A et al., 2024). Here we have used the updated version
238 DECSO v6.3 (van der A et al., 2024) for estimating simultaneously NO_x and NH₃ emissions using the
239 daily observations from TROPOMI and CrIS (referred to as multi-species DECSO). The main changes
240 of v6.3 include improving the sensitivity matrix calculation and using the latest Eulerian regional off-
241 line CTM CHIMERE v2020v3 (Menut et al., 2021) instead of CHIMERE v2013. In the CTM, we
242 employ the Copernicus Landcover 2019 data (Buchhorn et al., 2020), and the source sector distributions
243 of emissions obtained from HTAP v3 of 2018, which are also used as input emissions of other species
244 beside NO_x and NH₃. CHIMERE is driven by the operational meteorological forecast of the European
245 Centre for Medium-Range Weather Forecasts (ECMWF). Here we present the specific setting in
246 DECSO for NH₃ (referred to as DECSO-NH3).

247 To update NH₃ emissions based on the Kalman filter equations, one of the essential calculations is the
248 Kalman gain matrix (**K**) using the following equation:

$$249 \mathbf{K} = \mathbf{P}^f(t)\mathbf{H}[\mathbf{H}\mathbf{P}^f(t)\mathbf{H}^T + \mathbf{R}]^{-1} \quad (1)$$

250 \mathbf{P}^f is the error covariance matrix of the forecasted emissions at time t . \mathbf{H} is the sensitivity matrix
251 (Jacobian) describing how the NH₃ column concentration on a satellite footprint depends on gridded
252 NH₃ emissions. \mathbf{R} is the error covariance combining the observation error of tropospheric NH₃ columns,
253 the uncertainty of the CTM, and representation error introduced by projection of modelled columns on
254 the satellite footprint.

255 \mathbf{P}^f is parametrised based on an evaluation of the emission forecast error q , which is the error increase
256 during one time step of the forecast model. The emission forecast model is persistence, predicting that
257 the emission is equal to the analysis of the emissions from the previous day. We parametrize q of NH₃
258 following:

$$q = \varepsilon_{abs} \exp\left(-\frac{\varepsilon_{rel}}{\varepsilon_{abs}} e\right) + \varepsilon_{rel} e \quad (2)$$

ε_{abs} and ε_{rel} are the absolute and relative errors that are the dominating emission errors for low and high emissions respectively.

To determine ε_{abs} , ε_{rel} and also the covariance matrix \mathbf{R} for NH_3 , we follow the method described by Ding et al. (2017a) based on the analysis of Observation minus Forecast (OmF) and Observation minus Assimilation (OmA). The fitted ε_{abs} , ε_{rel} are 0.075×10^{15} molecule $\text{cm}^{-2} \text{h}^{-1}$ and 0.045. Note that \mathbf{R} is the variance of the observation error, the CTM model error and the representation error. Our analyses showed that the \mathbf{R} values are dominated by the satellite observation errors (σ_{obs}). The representation error can be neglected. We set the small contribution of model errors in \mathbf{R} to 0.5×10^{15} molecule cm^{-2} . To capture the quick changes of NH_3 emissions during the fertilizing seasons and give more weight to satellite observations with high values during the assimilation, we need to reduce their high observation errors for high values and keep the same observation errors for low values. By fitting NH_3 observation errors (σ_{obs}) against the observed columns C using all observations in 2020, we find a linear relation:

$$\bar{\sigma}_{obs} = \alpha C + b \quad (3)$$

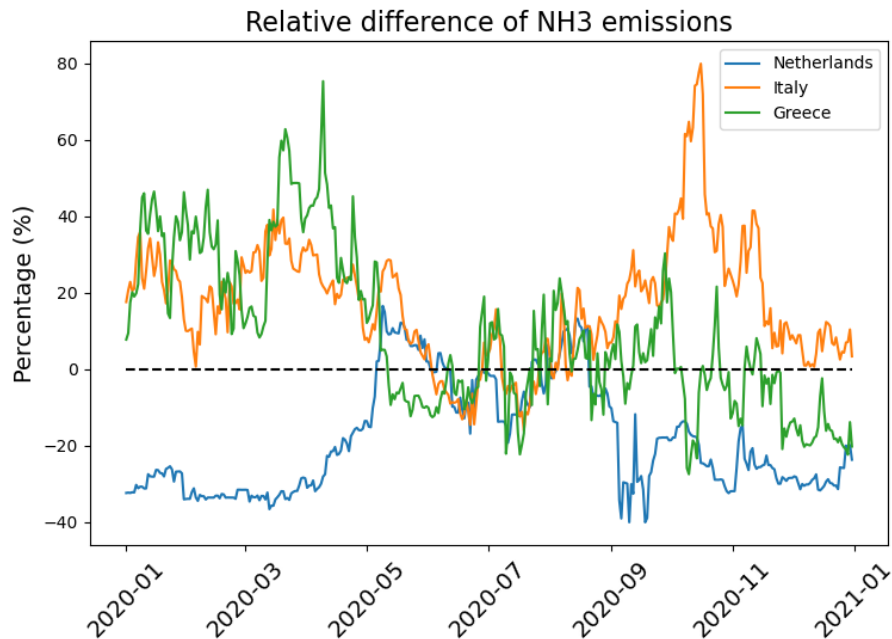
α is equal to 0.2 and b is equal to 1×10^{15} molecule cm^{-2} . If the given σ_{obs} is larger than $\alpha C + b$, we use Eq (3) for the observation error in \mathbf{R} .

We update NH_3 emissions only over land since there are almost no NH_3 emissions over oceans and seas.

As we mentioned, NH_3 reacts with sulfuric and nitric acids from SO_2 and NO_x to form $\text{PM}_{2.5}$. The changes in NO_x and SO_2 emissions will affect the concentration and removal of NH_3 in the atmosphere. Inaccurate emissions of NO_x and SO_2 will therefore affect the inversion of NH_3 emissions (Kuttippurath et al., 2024). To assess the sensitivity of NH_3 emissions derived with DECSO on NO_x and SO_2 emissions, we have run DECSO with different NO_x and SO_2 emissions (default emissions of HTAP v3 and doubling the emissions of HTAP v3 for SO_2 and NO_x) as input for the CTM. The results shows that the inversion of NH_3 emissions is not sensitive to the change of SO_2 emissions, but it is to NO_x emissions. In Europe, the impact of SO_2 emissions on NH_3 can be neglected nowadays due to the low SO_2 emissions (Luo et al., 2022), which have been reduced by 80% in 2020 compared to 2005 (EEA, 2023). The sensitivity tests indicate that up-to-date NO_x emissions are very important for the accurate inversion of NH_3 emissions. The monthly NO_x emissions of HTAP in 2018 and derived with DECSO in 2020 are quite different over the various countries (Figure S3). In 2020, due to the COVID-19 pandemic, NO_x emissions reduced compared to other years. van der A et al. (2024) has compared the seasonality of NO_x emissions of DECSO to other bottom-up inventories and showed individual temporal variability of industrial facilities is derived with DECSO in Europe, while bottom-up inventories use the same temporal profile per country per sector and no detailed information of the temporal changes of individual sources. We estimate NH_3 and NO_x emissions with DECSO simultaneously (the multi-specie

293 DECSO) from CrIS and TROPOMI on a daily basis. We use the DECSO-NH3 version to estimate only
 294 NH₃ emissions from CrIS and use NO_x emissions of HTAP v3 as input for the CTM. Figure 1 shows
 295 the difference of monthly NH₃ emissions in three countries (Netherlands, Italy and Greece) derived with
 296 the multi-species DECSO version and the DECSO-NH3 version. The derived NH₃ emissions all differ
 297 largely (up to ±40%) in winter and less in summer.

298



299

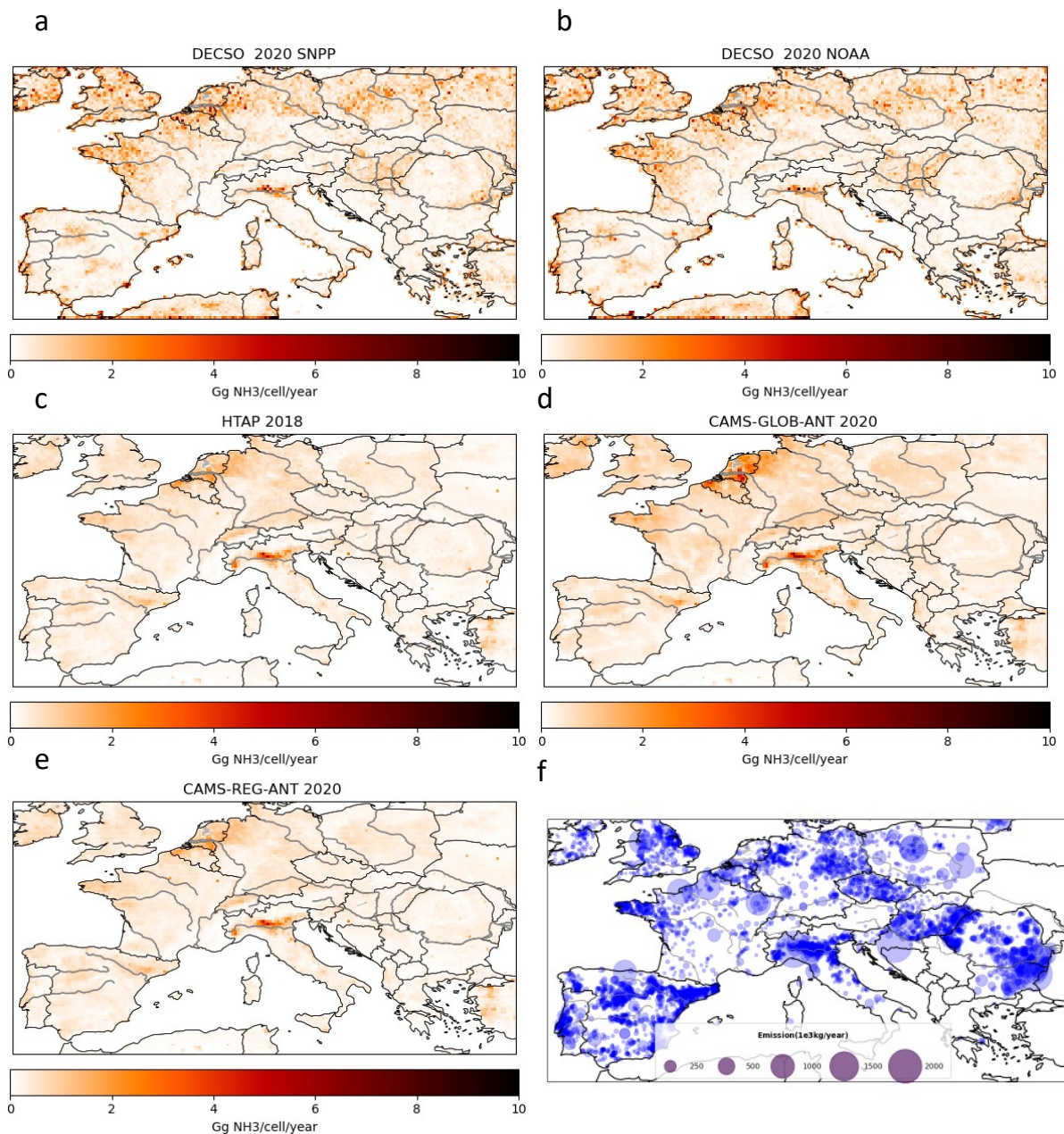
300 *Figure 1. The relative difference (multi-species DECSO minus DECSO-NH3) of NH₃ emissions between multi-species DECSO and*
 301 *DECSO-NH3. DECSO-NH3 means that only NH₃ emissions are derived with CrIS-NOAA-20. multi-species DECSO means that*
 302 *NH₃ and NO_x emissions are derived using CrIS-NOAA-20 and TROPOMI observations.*

303 3. Results

304 3.1 NH₃ emissions in Europe

305 We have run the multi-species DECSO version with NH₃ observations from CrIS-NOAA-20 and CrIS-
 306 SNPP respectively to estimate NH₃ emissions over the selected domain of Europe in 2020 (Figure 2),
 307 which is the only year with a full year overlap of NH₃ observations for these two satellites. The total
 308 NH₃ emissions over the study domain are 8.0 Tg/year from SNPP and 8.1 Tg /year from NOAA-20.
 309 The spatial distribution of the NH₃ emissions derived from the two satellites agrees well, with small
 310 differences (with a relative root mean square difference of 1.2%) resulting from deviations of the
 311 observed NH₃ columns. The spatial distribution of high NH₃ emissions derived from DECSO is similar
 312 to that of HTAP, CAMS-REG-ANT and CAMS-GLOB-ANT but with more local-scale variability and

313 hotspots. The total emissions of DECSO over the European domain are higher than HTAP (4.2 Tg/year),
 314 CAMS-REG-ANT (4.0 Tg/year) and CAMS-GLOB-ANT (5.9 Tg/year)



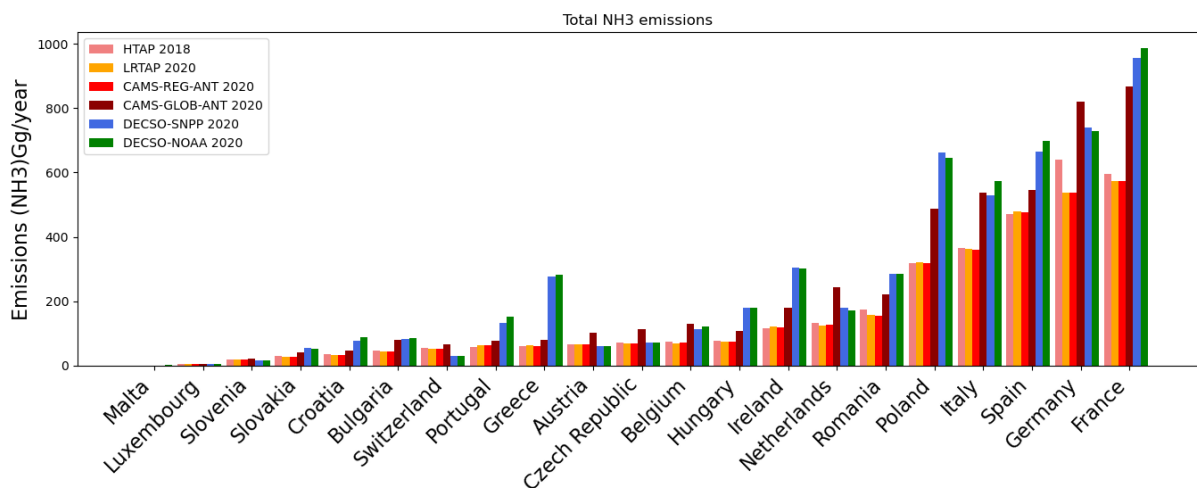
315

316 *Figure 2. NH₃ emission maps. NH₃ emissions derived with DECSO from (a) SNPP and (b) NOAA-20 in 2020. NH₃ emissions of*
 317 *(c) HTAP in 2018, (d) CAMS-GLOB-ANT in 2020 (e) CAMS-REG-ANT in 2020. (f) The registered point sources of E-PRTR in*
 318 *2017.*

319 The locations of high NH₃ emissions, especially in Po-Valley, Spain, Hungary and the east of Romania,
 320 shown in DECSO are highly correlated to the registered NH₃ point sources of E-PRTR which are from
 321 industrial facilities including livestock facilities but not from fertilizer applications. We see that
 322 emissions from the Netherlands are high in DECSO and the bottom-up inventories but are missing in
 323 the database of E-PRTR. For the countries in East Europe (e.g. Poland, Hungary, Romania), the NH₃

324 emissions derived with DECSO are much higher than from the bottom-up inventories. To assess the
 325 NH₃ emissions per country, we calculated the country total emissions (see Figure 3). The correlation
 326 coefficients of country totals from DECSO with the bottom-up inventories are all higher than 0.95. In
 327 general, the country totals of NH₃ emissions derived by DECSO from either NOAA-20 or SNPP are
 328 comparable to HTAP, LRTAP, CAMS-REG-ANT and CAMS-GLOB-ANT, with DECSO about 30%
 329 higher. HTAP, LRTAP and CAMS-REG-ANT have very similar emissions per country, while CAMS-
 330 GLOB-ANT shows higher emissions than the other three bottom-up inventories. Because HTAP v3
 331 uses annual emissions from CAMS-REG-ANT for Europe, the only difference between HTAP v3 and
 332 CAMS-REG-ANT is the difference in year. The input of CAMS-REG-ANT is mainly based on LRTAP.
 333 CAMS-GLOB-ANT is based on EDGAR and use different emission activities and factors compared to
 334 the other three bottom-up inventories. In the North part of Europe, for example Netherlands and
 335 Germany, DECSO results show lower NH₃ emissions than CAMS-GLOB-ANT but higher than HTAP,
 336 LRTAP and CAMS-REG-ANT.

337

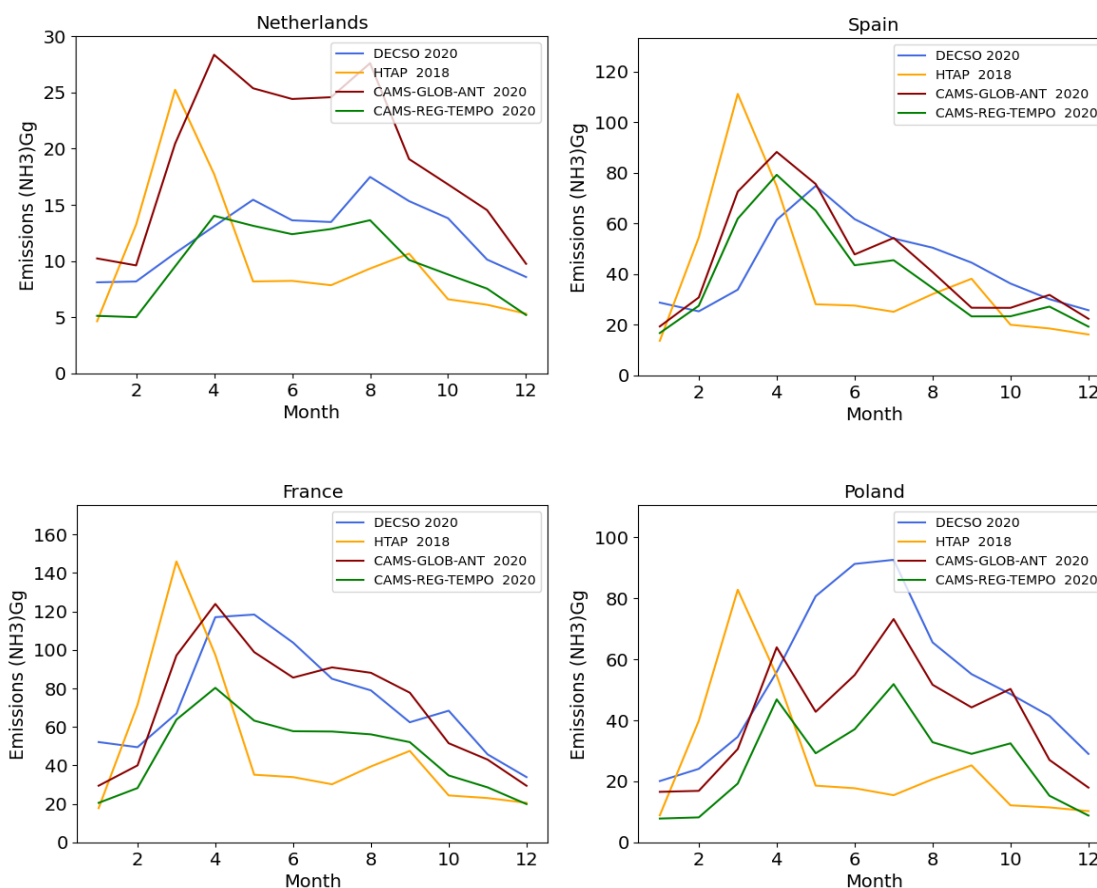


338

339 *Figure 3 Country totals of NH₃ emissions (Gg/year) according to database LRTAP in 2020, bottom-up inventories HTAP in*
 340 *2018, CAMS-REG-ANT in 2020, CAMS-GLOB-ANT in 2020 and the DECSO calculations from SNPP and NOAA-20 in 2020.*

341 To analyze the seasonality of NH₃ emissions derived from DECSO, we compare the monthly emissions
 342 of DECSO with bottom-up inventories. Figure 4 shows the monthly NH₃ emissions from DECSO,
 343 HTAP, CAMS-REG-TEMPO, and CAMS-GLOB-ANT of the Netherlands, Spain, France and Poland.
 344 We see that the seasonal cycle of NH₃ emissions of DECSO is closer to CAMS-GLOB-ANT. HTAP
 345 shows the exact same monthly variability for each country. CAMS-REG-TEMPO shows very similar
 346 monthly patterns to the ones reported by CAMS-GLOB-ANT as they are both using the same method
 347 to derive the temporal profiles for livestock and agricultural soil emissions (Guevara et al., 2021). In
 348 the Netherlands as an example for north Europe, the monthly NH₃ emissions of DECSO are lower than

349 CAMS-GLOB-ANT but very close to CAMS-REG-ANT. Two peaks of NH_3 emissions show up in
 350 April and August for CAMS emissions. This is also confirmed by the monthly surface concentrations
 351 measured by the MAN network (Figure S4). In Spain and France, the monthly emissions of DECSO
 352 are comparable to CAMS-GLOB-ANT. In the east part of Europe, such as Poland, DECSO estimates
 353 higher emissions. Note that in spring, when the NH_3 emissions are high due to fertilizer applications on
 354 farms, the NH_3 emissions derived with DECSO can suffer from a time lag due to insufficient
 355 observations (e.g. due to cloudiness, see Figure S5).



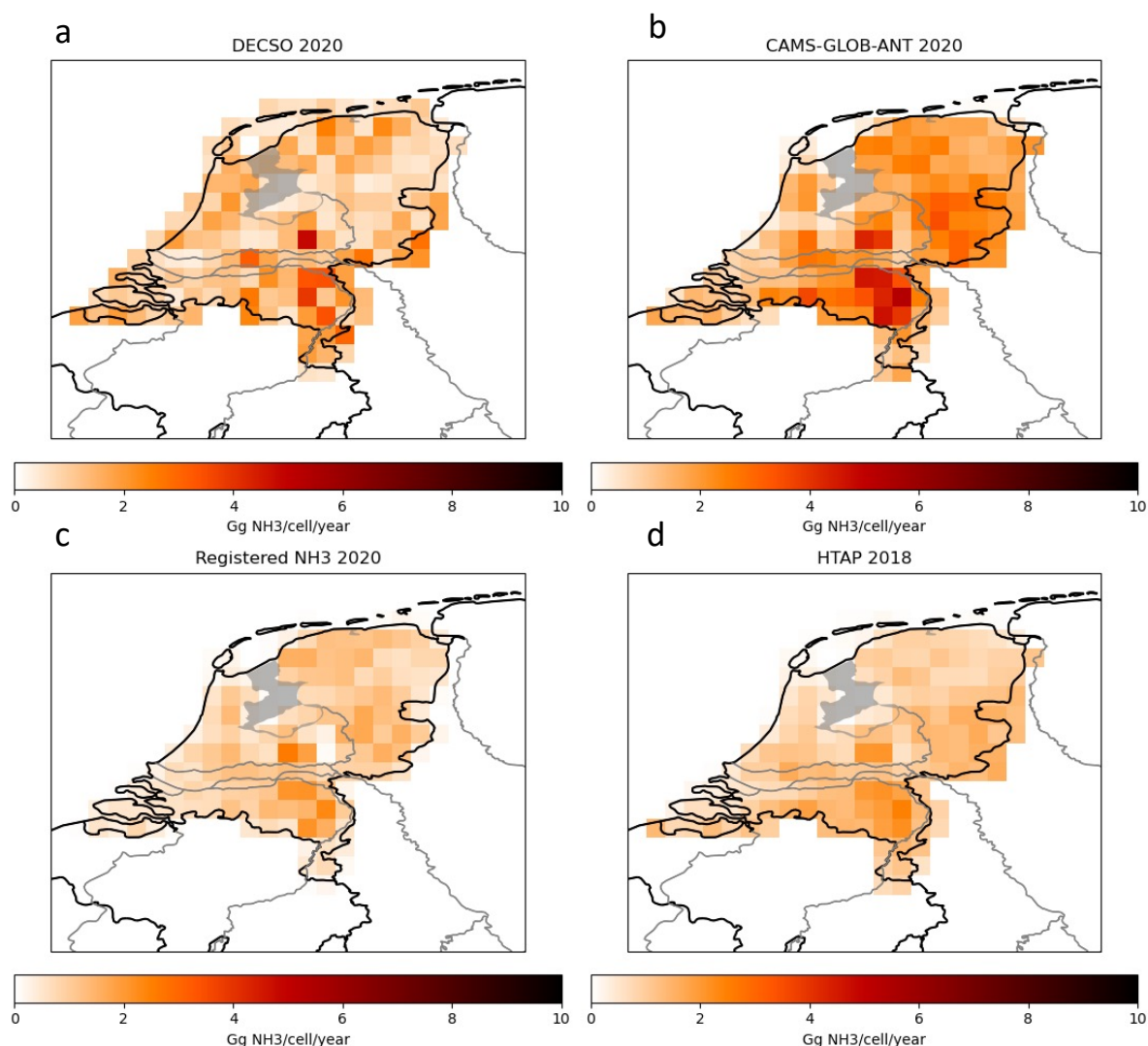
356
 357 *Figure 4 Monthly NH_3 emissions (Gg/month) of DECSO in 2020, HTAP in 2018, CAMS-REG-TEMPO in 2020 and CAMS-GLOB-*
 358 *TEMPO in 2020 for (a) the Netherlands, (b) Spain, (c) France and (d) Poland.*

359
 360 **3.2 Emissions in the Netherlands**

361 On the emission maps of Figure 2, we see that the Netherlands and Po-valley have the highest emission
 362 intensity of NH_3 . In this section, we focus our analysis on the Netherlands since it has the densest
 363 network for monitoring surface NH_3 concentrations and also a detailed emission inventory on a very
 364 high spatial resolution. The total emissions of the Netherlands estimated from the two satellites are very
 365 similar (Figure 3), but the spatial distributions show significant differences (Figure S6). One possible
 366 reason is that about 10% more observations are available from NOAA-20 than SNPP in 2020 (see Figure

367 S7). The number of valid observations is in general low at high latitudes (Figure S8). More observations
368 allow the detection of fast changes of NH₃ emissions from day to day. By averaging the emissions, the
369 information from both satellites is combined and improved the quality of the derived emissions due to
370 a doubling of the number of observations. We use the average of the results of DECSO-SNPP and
371 DECSO-NOAA-20 to get a better spatial distribution of NH₃ emissions derived from satellite
372 observations.

373 We compare the total NH₃ emissions of DECSO with CAMS-GLOB-ANT, HTAP and official national
374 NH₃ emissions of the Netherlands, which are 148, 230, 122 and 123 Gg/year respectively. DECSO is
375 lower than CAMS-GLOB-ANT but higher than HTAP and the official NH₃ emissions of the
376 Netherlands. Figure 5 shows the spatial distribution of each inventory in the Netherlands. We see that
377 DECSO captures the high emission areas and regional distribution over the country. The correlation
378 coefficients of the spatial distribution of NH₃ emissions between DECSO and the national emissions of
379 the Netherlands, HTAP v3, CAMS-GLOB-ANT are 0.87, 0.87 and 0.88 respectively. At the resolution
380 of the individual DECSO grid cells, 0.2° × 0.2° grid cell, the emission patterns show differences. This
381 may be due to uncertainties in the location of the emissions and displacements by up to one grid cell,
382 similar as for NO_x emissions (van der A et al., 2024). For example. the emission sources at the edge of
383 grid cells can be spread to the neighbouring grid cells.



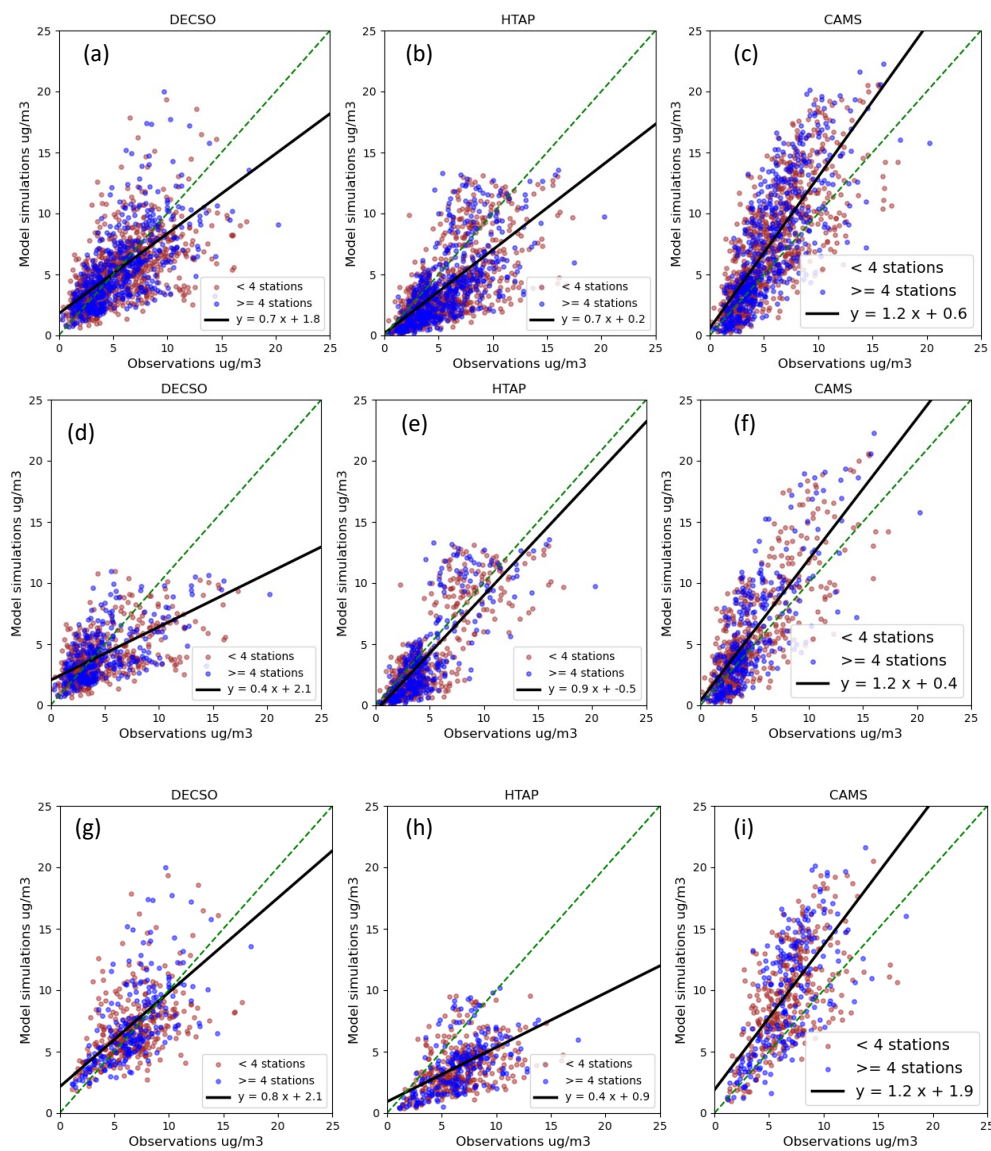
384

385 *Figure 5 NH₃ emissions in the Netherlands. (a) The averaged NH₃ emissions derived with DECSO from SNPP and NOAA-20.*
 386 *(b) NH₃ emissions of CAMS-GLOB-ANT in 2020. (c) The official national NH₃ emissions for the Netherlands in 2020 (from*
 387 *emissieregistratie.nl). (d) NH₃ emissions of HTAP in 2018.*

388 To further assess the DECSO results using in-situ observations from both LML and MAN networks in
 389 the Netherlands, we have conducted three runs of CHIMERE for the year 2020 using NH₃ emissions
 390 from DECSO in 2020, HTAP in 2018 and CAMS-GLOB-ANT in 2020 over the European domain
 391 (same as the setup of DECSO). To compare to the surface NH₃ measurement from the MAN network,
 392 we calculate the monthly average of surface NH₃ concentrations from the model simulations. Figure 6
 393 (a-c) shows the scatter plots of monthly NH₃ concentrations of model simulations against observations
 394 for the whole year. We see that modelled NH₃ concentrations with the HTAP emissions are
 395 underestimated and those with the CAMS-GLOB-ANT emissions are overestimated compared to in-
 396 situ observations. The modelled NH₃ concentrations with DECSO emissions have the lowest absolute
 397 bias (modelled concentration minus in-situ observations of the MAN network) (Figure 7). The
 398 performance of model simulations is better in summer months (April to September) than in winter

399 months (October-March). In winter months, few cloud-free satellite observations are available for the
 400 Netherlands. For DECSO, the scatter plot looks more spread out than in summer months (Figure 6d-i).
 401 In summer months, the NH₃ concentrations with CAMS-GLOB-ANT are largely overestimated and
 402 with HTAP are largely underestimated, while DECSO has a lower bias compared to the other two. Note
 403 that in the grid cells, the number of stations can vary from 1 to 16. If we select grid cells with more than
 404 3 sites, DECSO shows better spatial correlation with in-situ observations than for the other two
 405 inventories and the lowest bias (Figure 7 and Table 2).

406

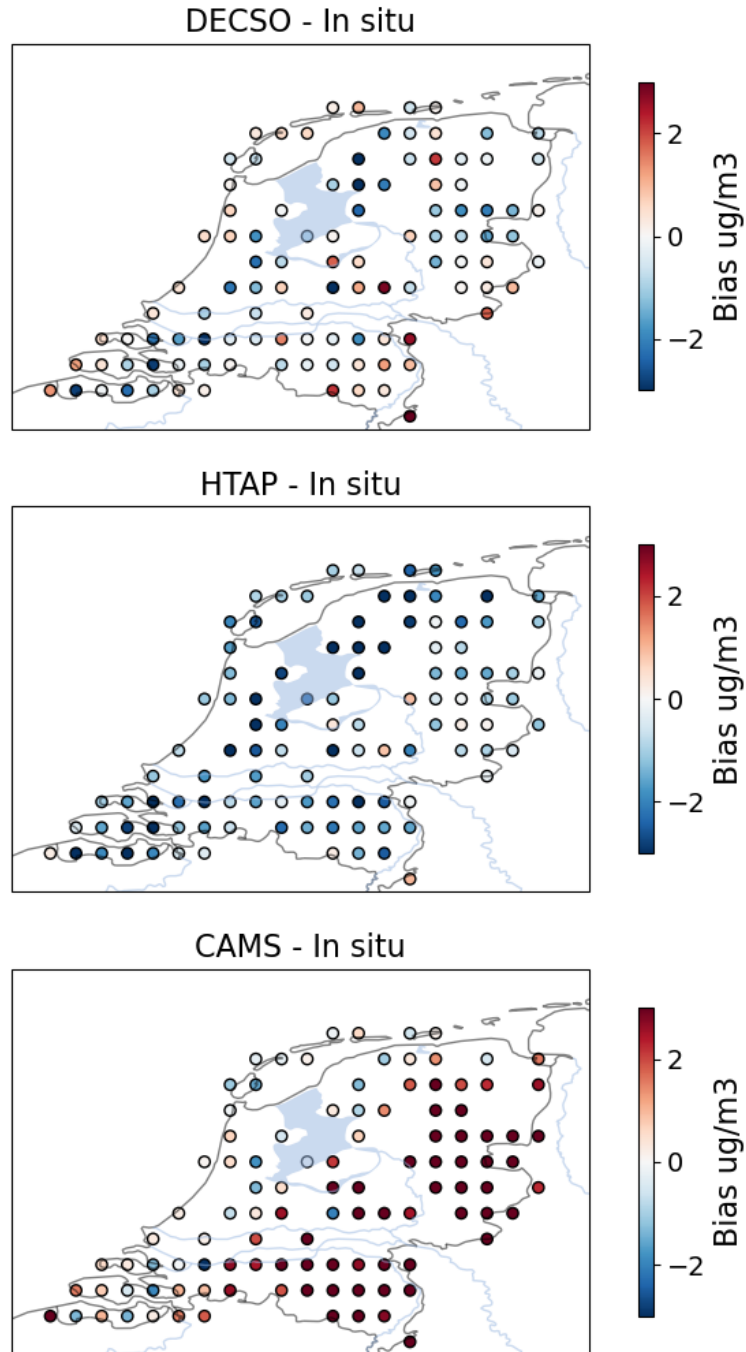


407

408 *Figure 6. Scatter plots of observations from the MAN network with NH₃ surface concentrations from model simulations with*
 409 *NH₃ emissions from DECSO (left column), HTAP (middle column) and CAMS-GLOB-ANT (right column). (a-c) The scatter plot*
 410 *of data for the whole year for all sites. (d-f) The scatter plot of the data in winter months (October to March). (g-i) The*
 411 *scatter plot of the data in summer months (April to September). Each point presents the model grid cells having the in-situ*

412 observations. The red dots mean there are less than four in-situ sites in the grid cells. The blue dots mean there are at least
413 four in-situ sites in the grid cell. The fitted black line is for grid cells with at least four in-situ sites.

414



415
416 *Figure 7. Bias of the model simulated surface concentrations with NH_3 emissions from DECISO (left column), HTAP (middle*
417 *column) and CAMS-GLOB-ANT (right column) compared to the in-situ observations from the MAN network.*

418

419 *Table 2. The spatial and temporal correlation coefficients and the bias of monthly mean simulated NH₃ surface concentration*
 420 *using DECSO, HTAP and CAMS-GLOB-ANT NH₃ emissions against observations of the MAN network for grid cells with more*
 421 *than three measurement locations.*

	Temporal correlation coefficient	Spatial correlation coefficient	Bias (ug/m ³)	RMSE (ug/m ³)
DECSO	0.64	0.73	-0.2	2.6
HTAP v3	0.70	0.70	-1.9	3.0
CAMS-GLOB-ANT	0.82	0.70	-0.3	3.8

422

423

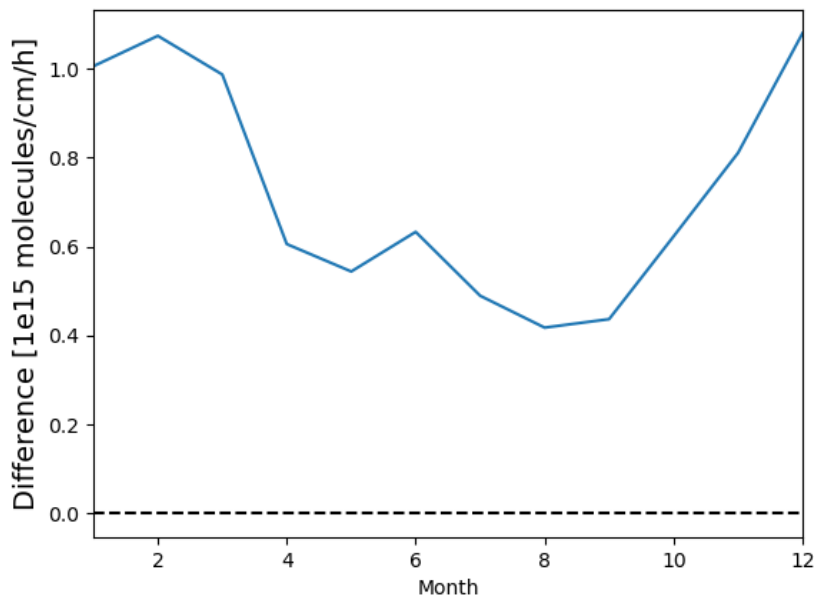
424 The LML network has six sites measuring surface NH₃ concentrations, which are provided every hour.
 425 Since the difference in our model simulations is only due to the monthly input emissions of NH₃, we
 426 calculate monthly average NH₃ observations for the six sites to compare with the modelled monthly
 427 averaged concentrations. The comparison shows that the model simulations using the DECSO NH₃
 428 emissions have similar performance as bottom-up inventories (Figure S9 and S10). The correlations of
 429 modelled monthly NH₃ concentration using DECSO and CAMS-GLOB-ANT emissions with the
 430 observations from the LML network are better than that of HTAP, while CAMS-GLOB-ANT has the
 431 lowest bias. Based on these six sites, the comparison shows that the model result using DECSO is very
 432 comparable with that using CAMS-GLOB-ANT.

433

434 3.3 Uncertainties and bias of NH₃ emissions

435 One advantage of DECSO is that a standard deviation of derived emissions is also calculated per grid
 436 cell on a daily basis according to the Kalman filter equations. As described by van der A et al. (2024), the
 437 derived errors in the emissions are correlated in time linked to the assumption of the persistent emission
 438 forecast model. The autocorrelation effects can be neglected after about one week up to ten days. We
 439 follow the autocorrelation function presented by van der A et al. (2024) to calculate the monthly variance
 440 of NH₃ emissions. The monthly variance of NH₃ emissions for each grid cell in the study domain varies
 441 from 17% to 58%. For the Netherlands, the precision (random uncertainty) of the monthly emissions is
 442 about 20% and the precision of the annual total is about 5%.

443 A bias in satellite derived emissions can be introduced due to the linearisation of the averaging kernels
 444 (Sitwell et al., 2022). The CrIS ammonia observations are retrieved in logarithm space together with
 445 logarithmic averaging kernels. As discussed by Sitwell et al. (2022), either using the logarithmic
 446 averaging kernel or the linearized averaging kernel introduces a bias when applying them to the model
 447 simulated profiles. The logarithmic averaging kernels cause problems when the model profiles are zero
 448 at any point in the profile and lead to a positive bias in emission estimates. Linearized averaging kernels
 449 may introduce a negative bias in emissions when there is a large difference between the model profile
 450 and the a priori profile used in the retrieval.



451

452 *Figure 8. The absolute change of monthly NH₃ emissions (molecule/cm²/h) if there is a positive bias of 5×10^{15}*
 453 *molecule/cm² of each NH₃ column observation.*

454 To assess how the biases in satellite NH₃ observations affect emissions derived by DECSO, we have
 455 done two simple bias tests. For the first test, the NH₃ columns of CrIS on NOAA-20 are increased by
 456 20%, a positive relative bias for the satellite observations. The annual emissions of NH₃ with the
 457 introduced bias increase by 27% for the European domain. It seems that the introduced bias has a higher
 458 impact on emissions in winter than in summer. The relative bias on emissions can be as high as 50% in
 459 winter. The change of emissions in summer becomes even negative probably because NH₃ column
 460 concentrations can show a large variation from day to day. When the NH₃ columns are very high on
 461 one day and next drop to a very low value, the absolute change in concentration is larger than the
 462 original situation without introduced bias. This will lead to a larger decrease in the updated emissions
 463 and can result in a negative change of emissions. For the second test, an absolute bias of 5×10^{15}
 464 molecule/cm² is added to each NH₃ column observation of CrIS on NOAA-20. Figure 8 shows the
 465 increase of NH₃ emissions caused by the absolute bias introduced in the satellite observations. We see

466 that the increase is doubled in winter compared to summer, because the lifetime in winter is longer than
467 in summer. The averaged effective lifetime calculated with DECSO is about 10 hours in winter and 5
468 hours in summer. With the same bias of NH₃ columns, the impact on emissions is larger in winter than
469 in summer.

470

471 4. Discussion and Conclusion

472 To derive NH₃ emissions from satellite data, we presented an updated version of the DECSO algorithm
473 with specific settings for NH₃. Together with the improved the DECSO version for NO_x of van der A
474 et al. (2024), we have the multi-species DECSO version to update NO_x and NH₃ emissions
475 simultaneously. In general, the removal of NH₃ in the atmosphere is affected by the amount of NO_x and
476 SO₂ emissions. For the study domain of Europe, our sensitivity study shows that the influence of
477 changes in NO_x emissions need to be considered in the inversion of NH₃ emissions in DECSO. The
478 impact of SO₂ emissions is very small and can be neglected since the SO₂ emissions are usually low in
479 Europe. Thus, to derive NH₃ emissions and to analyze the seasonal cycle and trend of NH₃ emissions
480 from satellite observations over Europe, it is recommended to include updated NO_x emissions in the
481 inversion calculation of NH₃ emissions in DECSO. For regions with high SO₂ emissions, it is necessary
482 to consider if the SO₂ emissions are changing rapidly and are up-to-date in the inversion.

483 The error covariances of the updated daily NH₃ emissions per grid cell are provided during the
484 calculation in DECSO. Considering the autocorrelations introduced by the assumption of the
485 persistency emission model, the calculated monthly error on NH₃ emissions for each grid cell in the
486 study domain varies from 17% to 58%. The yearly error per grid cell is about 5 ~ 15%. The sensitivity
487 tests for retrieval biases shows that with an introduced constant relative and absolute bias in NH₃
488 retrievals, the resulting bias in emissions derived with DECSO shows a seasonal variability with a peak
489 in winter. This means the algorithm is more sensitive to a bias in the observations during wintertime.

490 The total NH₃ emissions in our European domain derived from NH₃ observations of SNPP and NOAA-
491 20 are 8.0 Tg/year and 8.1 Tg/year respectively with a precision of about 5 - 17 % per grid cell/year.
492 The difference in country total emissions derived from the two satellites is very small. However, the
493 details of the spatial distribution of emissions derived from both satellites are different over the north
494 part of the domain, such as the Netherlands. This may be due to the varying number of observations per
495 region per year from the two satellites. An average of the emissions derived from both satellites leads
496 to an improved spatial distribution compared to the emissions from the individual satellite. The spatial
497 distribution of derived NH₃ emissions is similar to the bottom-up inventories, but DECSO emissions
498 are in general higher. The annual total emissions derived by DECSO for the whole domain is larger than
499 the bottom-up inventories (LRTAP, HTAP, CAMS-REG-ANT and CAMS-GLOB-ANT). The
500 comparison of country total emissions shows that DECSO gives higher NH₃ emissions for the countries

501 in East Europe than the bottom-up inventories. In addition, DECSO results show higher sources in
502 Spain, Hungary and the east of Romania. This is in line with the registered point sources of E-PRTR.
503 The seasonal cycle of the emissions of DECSO are comparable to CAMS-GLOB-ANT, while HTAP
504 uses the same seasonal cycle for each country in Europe. The analysis indicates that DECSO can be
505 used to estimate NH₃ over a long period for the trend study. The retrieval product of NH₃ from SNPP
506 ends in May 2021. Because of the insignificant differences in NH₃ emissions derived from the two
507 satellites for the overlap year 2020, the trends analysis can be continued by using the NH₃ data from
508 NOAA-20 (Figure S11). We have shown the importance of the impact of NO_x emissions on the inversion
509 of NH₃ emissions. Since the NO_x emissions derived from TROPOMI have good agreement with CAMS-
510 REG-ANT, as shown by van der A et al. (2024), the NO_x emissions from CAMS-REG-ANT can be
511 used for the years before 2019 in trend studies of NH₃ emissions over Europe. For the Netherlands,
512 model simulations using NH₃ emissions from DECSO, HTAP and CAMS-GLOB-ANT are compared
513 to in-situ observations from the MAN and LML networks. In general, the simulation using DECSO
514 emissions has a lower bias, but also a lower temporal correlation compared to CAM-GLOB-ANT. The
515 performance of model simulations with DECSO is better in summer than in winter. Both the bias and
516 spatial correlation between model simulations using DECSO emissions and the MAN in-situ
517 observations are higher than CAMS-GLOB-ANT for grid cells including more than 3 measurement
518 sites. We conclude that satellite-derived emissions derived with DECSO show a comparable temporal
519 and spatial distribution as bottom-up inventories. The emissions derived from satellite observations can
520 provide fully independent information on emissions for verifying the bottom-up inventories. With the
521 global coverage of satellite observations, DECSO can be easily applied to different regions. After
522 validation of DECSO over regions like Europe, where there is sufficient information of emissions, the
523 added value of DECSO for deriving NH₃ emissions is to provide NH₃ emissions over regions with
524 limited local information of NH₃ emissions.

525

526 Data

527 The CrIS NH₃ data v1.6.4 of SNPP and NOAA-20 created by Environment and Climate Change Canada
528 are currently publicly available upon request (mark.shephard@canada.ca) at
529 https://hpfx.collab.science.gc.ca/~mas001/satellite_ext/cris/snpp/nh3/v1_6_4.

530 The TROPOMI NO₂ data version 2.4 are available via the Copernicus website
531 <https://dataspace.copernicus.eu/> and via the TEMIS website
532 <https://www.temis.nl/airpollution/no2.php> (last access: 02 August 2024)
533 (<https://doi.org/10.5270/S5P-9bnp8q8TS15>).

534 The NH₃ and NO_x emissions of DECSO v6.3 are available on the GlobEmission website
535 <https://www.temis.nl/emissions/data.php>.
536 HTAP v3 dataset are available on https://edgar.jrc.ec.europa.eu/dataset_htap_v3
537 The European emissions data sets for countries NEC, LRTAP and large facilities E-PRTR are available
538 on the website <https://www.eea.europa.eu/en/analysis> of the EEA.
539 The CAMS databases CAMS-REG-ANT v5.1, CAMS-GLOB-ANT, CAMS-TEMPO are available on the
540 ECCAD website <https://permalink.aeris-data.fr>.
541 The NH₃ observation data from the LML network are available on the RIVM website
542 <https://data.rivm.nl/data/luchtmeetnet/>.
543 The NH₃ observation data from the MAN network are available at <https://man.rivm.nl>.
544 The Dutch registered NH₃ emissions are available at <https://data.emissieregistratie.nl/export>

545

546

547 Author contribution

548 JD developed the inversion algorithm of NH₃, performed all emission inversions, conducted the
549 analysis and wrote the manuscript. RA and JD made the improvement of the inversion algorithm of
550 NO_x. HE developed the superobservation code. ED provided the code for a linearization of the
551 averaging kernels of CrIS. MS provided the CrIS data. RWK provided the NH₃ observation data from the
552 MAN and LML networks. MGV provided the CAMS-TEMPO profiles. LT provided suggestions during the
553 research. All authors contributed to the reviewing and editing of the manuscript.

554

555

556 Acknowledgments

557 This the work was financed by the Sentinel EO-based Emission and Deposition Service (SEEDS, Grant
558 ID 101004318) project that has received funding from the European Union's Horizon 2020 research
559 and innovation programme. Part of the work was funded by the Nationaal Kennisprogramma Stikstof
560 (NKS) of the Dutch Ministry of Agriculture, Nature and Food Quality.

561

562

563 References

564

565 Adams, C., McLinden, C. A., Shephard, M. W., Dickson, N., Dammers, E., Chen, J., Makar, P.,
566 Cady-Pereira, K. E., Tam, N., Kharol, S. K., Lamsal, L. N., and Krotkov, N. A.: Satellite-derived
567 emissions of carbon monoxide, ammonia, and nitrogen dioxide from the 2016 Horse River
568 wildfire in the Fort McMurray area, *Atmos. Chem. Phys.*, 19, 2577-2599, 10.5194/acp-19-
569 2577-2019, 2019.

570

571 Backes, A., Aulinger, A., Bieser, J., Matthias, V., and Quante, M.: Ammonia emissions in
572 Europe, part I: Development of a dynamical ammonia emission inventory, *Atmospheric
573 Environment*, 131, 55-66, <https://doi.org/10.1016/j.atmosenv.2016.01.041>, 2016a.

574

575 Backes, A. M., Aulinger, A., Bieser, J., Matthias, V., and Quante, M.: Ammonia emissions in
576 Europe, part II: How ammonia emission abatement strategies affect secondary aerosols,
577 *Atmospheric Environment*, 126, 153-161, <https://doi.org/10.1016/j.atmosenv.2015.11.039>,
578 2016b.

579

580 Beer, R., Shephard, M. W., Kulawik, S. S., Clough, S. A., Eldering, A., Bowman, K. W., Sander,
581 S. P., Fisher, B. M., Payne, V. H., Luo, M., Osterman, G. B., and Worden, J. R.: First satellite
582 observations of lower tropospheric ammonia and methanol, *Geophysical Research Letters*,
583 35, <https://doi.org/10.1029/2008GL033642>, 2008.

584

585 Behera, S. N., Sharma, M., Aneja, V. P., and Balasubramanian, R.: Ammonia in the
586 atmosphere: a review on emission sources, atmospheric chemistry and deposition on
587 terrestrial bodies, *Environmental Science and Pollution Research*, 20, 8092-8131,
588 10.1007/s11356-013-2051-9, 2013.

589

590 Berkhout, A. J. C., Swart, D. P. J., Volten, H., Gast, L. F. L., Haaima, M., Verboom, H., Stefess,
591 G., Hafkenscheid, T., and Hoogerbrugge, R.: Replacing the AMOR with the miniDOAS in the
592 ammonia monitoring network in the Netherlands, *Atmos. Meas. Tech.*, 10, 4099-4120,
593 10.5194/amt-10-4099-2017, 2017.

594

595 Beusen, A. H. W., Bouwman, A. F., Heuberger, P. S. C., Van Drecht, G., and Van Der Hoek, K.
596 W.: Bottom-up uncertainty estimates of global ammonia emissions from global agricultural
597 production systems, *Atmospheric Environment*, 42, 6067-6077,
598 <https://doi.org/10.1016/j.atmosenv.2008.03.044>, 2008.

599

600 Boersma, K. F., Vinken, G. C. M., and Eskes, H. J.: Representativeness errors in comparing
601 chemistry transport and chemistry climate models with satellite UV-Vis tropospheric
602 column retrievals, *Geosci. Model Dev.*, 9, 875-898, 10.5194/gmd-9-875-2016, 2016.

603

604 Buchhorn, M., Smets, B., Bertels, L., De Roo, B., Lesiv, M., Tsendbazar, N.-E., Herold, M., and
605 Fritz, S.: Copernicus Global Land Service: Land Cover 100m: collection 3: epoch 2019: Globe,
606 10.5281/zenodo.3939050, 2020.

607

608 Cao, H., Henze, D. K., Shephard, M. W., Dammers, E., Cady-Pereira, K., Alvarado, M.,
609 Lonsdale, C., Luo, G., Yu, F., Zhu, L., Danielson, C. G., and Edgerton, E. S.: Inverse modeling of
610 NH₃ sources using CrIS remote sensing measurements, *Environmental Research Letters*, 15,
611 104082, 10.1088/1748-9326/abb5cc, 2020.
612
613 Cao, H., Henze, D. K., Zhu, L., Shephard, M. W., Cady-Pereira, K., Dammers, E., Sitwell, M.,
614 Heath, N., Lonsdale, C., Bash, J. O., Miyazaki, K., Flechard, C., Fauvel, Y., Kruit, R. W.,
615 Feigenspan, S., Brümmer, C., Schrader, F., Twigg, M. M., Leeson, S., Tang, Y. S., Stephens, A. C.
616 M., Braban, C., Vincent, K., Meier, M., Seitler, E., Geels, C., Ellermann, T., Sanocka, A., and
617 Capps, S. L.: 4D-Var Inversion of European NH₃ Emissions Using CrIS NH₃ Measurements and
618 GEOS-Chem Adjoint With Bi-Directional and Uni-Directional Flux Schemes, *Journal of*
619 *Geophysical Research: Atmospheres*, 127, e2021JD035687,
620 <https://doi.org/10.1029/2021JD035687>, 2022.
621
622 Chen, Y., Shen, H., Kaiser, J., Hu, Y., Capps, S. L., Zhao, S., Hakami, A., Shih, J. S., Pavur, G. K.,
623 Turner, M. D., Henze, D. K., Resler, J., Nenes, A., Napelenok, S. L., Bash, J. O., Fahey, K. M.,
624 Carmichael, G. R., Chai, T., Clarisse, L., Coheur, P. F., Van Damme, M., and Russell, A. G.: High-
625 resolution hybrid inversion of IASI ammonia columns to constrain US ammonia emissions
626 using the CMAQ adjoint model, *Atmos. Chem. Phys.*, 21, 2067-2082, 10.5194/acp-21-2067-
627 2021, 2021.
628
629 Clarisse, L., Clerbaux, C., Dentener, F., Hurtmans, D., and Coheur, P.-F.: Global ammonia
630 distribution derived from infrared satellite observations, *Nature Geoscience*, 2, 479-483,
631 10.1038/ngeo551, 2009.
632
633 Crippa, M., Guizzardi, D., Muntean, M., Schaaf, E., Dentener, F., van Aardenne, J. A., Monni,
634 S., Doering, U., Olivier, J. G. J., Pagliari, V., and Janssens-Maenhout, G.: Gridded emissions of
635 air pollutants for the period 1970–2012 within EDGAR v4.3.2, *Earth Syst. Sci. Data*, 10, 1987-
636 2013, 10.5194/essd-10-1987-2018, 2018.
637
638 Crippa, M., Guizzardi, D., Butler, T., Keating, T., Wu, R., Kaminski, J., Kuenen, J., Kurokawa, J.,
639 Chatani, S., Morikawa, T., Pouliot, G., Racine, J., Moran, M. D., Klimont, Z., Manseau, P. M.,
640 Mashayekhi, R., Henderson, B. H., Smith, S. J., Suchyta, H., Muntean, M., Solazzo, E., Banja,
641 M., Schaaf, E., Pagani, F., Woo, J. H., Kim, J., Monforti-Ferrario, F., Pisoni, E., Zhang, J., Niemi,
642 D., Sassi, M., Ansari, T., and Foley, K.: The HTAP_v3 emission mosaic: merging regional and
643 global monthly emissions (2000–2018) to support air quality modelling and policies, *Earth*
644 *Syst. Sci. Data*, 15, 2667-2694, 10.5194/essd-15-2667-2023, 2023.
645
646 Dammers, E., McLinden, C. A., Griffin, D., Shephard, M. W., Van Der Graaf, S., Lutsch, E.,
647 Schaap, M., Gainairu-Matz, Y., Fioletov, V., Van Damme, M., Whitburn, S., Clarisse, L., Cady-
648 Pereira, K., Clerbaux, C., Coheur, P. F., and Erisman, J. W.: NH₃ emissions from large point
649 sources derived from CrIS and IASI satellite observations, *Atmos. Chem. Phys.*, 19, 12261-
650 12293, 10.5194/acp-19-12261-2019, 2019.
651
652 Ding, J., van der A, R. J., Mijling, B., and Levelt, P. F.: Space-based NO_x emission estimates
653 over remote regions improved in DECSO, *Atmos. Meas. Tech.*, 10, 925-938, 10.5194/amt-10-
654 925-2017, 2017a.

655
656 Ding, J., van der A, R. J., Mijling, B., Levelt, P. F., and Hao, N.: NO_x emission estimates during
657 the 2014 Youth Olympic Games in Nanjing, *Atmos. Chem. Phys.*, 15, 9399-9412,
658 10.5194/acp-15-9399-2015, 2015.
659
660 Ding, J., van der A, R., Mijling, B., de Laat, J., Eskes, H., and Boersma, K. F.: NO_x emissions in
661 India derived from OMI satellite observations, *Atmospheric Environment: X*, 14, 100174,
662 <https://doi.org/10.1016/j.aeaoa.2022.100174>, 2022.
663
664 Ding, J., van der A, R. J., Eskes, H. J., Mijling, B., Stavrou, T., van Geffen, J. H. G. M., and
665 Veefkind, J. P.: NO_x Emissions Reduction and Rebound in China Due to the COVID-19 Crisis,
666 *Geophysical Research Letters*, 47, e2020GL089912, 10.1029/2020GL089912, 2020.
667
668 Ding, J., Miyazaki, K., van der A, R. J., Mijling, B., Kurokawa, J. I., Cho, S., Janssens-Maenhout,
669 G., Zhang, Q., Liu, F., and Levelt, P. F.: Intercomparison of NO_x emission inventories over East
670 Asia, *Atmos. Chem. Phys.*, 17, 10125-10141, 10.5194/acp-17-10125-2017, 2017b.
671
672 EEA: Emissions of the main air pollutants in Europe,
673 [https://www.eea.europa.eu/en/analysis/indicators/emissions-of-the-main-](https://www.eea.europa.eu/en/analysis/indicators/emissions-of-the-main-air?activeAccordion=ecdb3bcf-bbe9-4978-b5cf-0b136399d9f8)
674 [air?activeAccordion=ecdb3bcf-bbe9-4978-b5cf-0b136399d9f8](https://www.eea.europa.eu/en/analysis/indicators/emissions-of-the-main-air?activeAccordion=ecdb3bcf-bbe9-4978-b5cf-0b136399d9f8), last access: 3 April, 2024.
675
676 EPRT: European Pollutant Release and Transfer Register, database version v4.2 [dataset],
677 <http://prtr.ec.europa.eu/>, 2012.
678
679 Erisman, J. W., Sutton, M. A., Galloway, J., Klimont, Z., and Winiwarter, W.: How a century of
680 ammonia synthesis changed the world, *Nature Geoscience*, 1, 636-639, 10.1038/ngeo325,
681 2008.
682
683 Erisman, J. W., Galloway, J. N., Seitzinger, S., Bleeker, A., Dise, N. B., Petrescu, A. M. R., Leach,
684 A. M., and de Vries, W.: Consequences of human modification of the global nitrogen cycle,
685 *Philosophical Transactions of the Royal Society B: Biological Sciences*, 368, 20130116,
686 doi:10.1098/rstb.2013.0116, 2013.
687
688 Eskes, H. J. and Eichmann, K.-U.: S5P Mission Performance Centre Nitrogen Dioxide
689 [L2__NO2__] Readme, Tech.rep., ESA, [https://sentinel.esa.int/documents/247904/3541451/Sentinel-5P-Nitrogen-Dioxide-Level-2-](https://sentinel.esa.int/documents/247904/3541451/Sentinel-5P-Nitrogen-Dioxide-Level-2-Product-Readme-File)
690 [Product-Readme-File](https://sentinel.esa.int/documents/247904/3541451/Sentinel-5P-Nitrogen-Dioxide-Level-2-Product-Readme-File), 2022.
691
692
693 Galloway, J. N., Townsend, A. R., Erisman, J. W., Bekunda, M., Cai, Z., Freney, J. R., Martinelli,
694 L. A., Seitzinger, S. P., and Sutton, M. A.: Transformation of the Nitrogen Cycle: Recent
695 Trends, Questions, and Potential Solutions, *Science*, 320, 889-892,
696 doi:10.1126/science.1136674, 2008.
697
698 Ge, X., Schaap, M., Kranenburg, R., Segers, A., Reinds, G. J., Kros, H., and de Vries, W.:
699 Modeling atmospheric ammonia using agricultural emissions with improved spatial
700 variability and temporal dynamics, *Atmos. Chem. Phys.*, 20, 16055-16087, 10.5194/acp-20-
701 16055-2020, 2020.

702
703 Gu, B., Zhang, L., Van Dingenen, R., Vieno, M., Van Grinsven, H. J., Zhang, X., Zhang, S., Chen,
704 Y., Wang, S., Ren, C., Rao, S., Holland, M., Winiwarter, W., Chen, D., Xu, J., and Sutton, M. A.:
705 Abating ammonia is more cost-effective than nitrogen oxides for mitigating
706 PM_{2.5} air pollution, *Science*, 374, 758-762, doi:10.1126/science.abf8623, 2021.
707
708 Guevara, M., Jorba, O., Tena, C., Denier van der Gon, H., Kuenen, J., Elguindi, N., Darras, S.,
709 Granier, C., and Pérez García-Pando, C.: Copernicus Atmosphere Monitoring Service
710 TEMPORal profiles (CAM5-TEMPO): global and European emission temporal profile maps for
711 atmospheric chemistry modelling, *Earth Syst. Sci. Data*, 13, 367-404, 10.5194/essd-13-367-
712 2021, 2021.
713
714 Han, Y., Revercomb, H., Crompton, M., Gu, D., Johnson, D., Mooney, D., Scott, D., Strow, L.,
715 Bingham, G., Borg, L., Chen, Y., DeSloover, D., Esplin, M., Hagan, D., Jin, X., Knuteson, R.,
716 Motteler, H., Predina, J., Suwinski, L., Taylor, J., Tobin, D., Tremblay, D., Wang, C., Wang, L.,
717 Wang, L., and Zavyalov, V.: Suomi NPP CrIS measurements, sensor data record algorithm,
718 calibration and validation activities, and record data quality, *Journal of Geophysical*
719 *Research: Atmospheres*, 118, 12,734-712,748, <https://doi.org/10.1002/2013JD020344>,
720 2013.
721
722 Hoesly, R. M., Smith, S. J., Feng, L., Klimont, Z., Janssens-Maenhout, G., Pitkanen, T., Seibert,
723 J. J., Vu, L., Andres, R. J., Bolt, R. M., Bond, T. C., Dawidowski, L., Kholod, N., Kurokawa, J. I.,
724 Li, M., Liu, L., Lu, Z., Moura, M. C. P., O'Rourke, P. R., and Zhang, Q.: Historical (1750–2014)
725 anthropogenic emissions of reactive gases and aerosols from the Community Emissions Data
726 System (CEDS), *Geosci. Model Dev.*, 11, 369-408, 10.5194/gmd-11-369-2018, 2018.
727
728 Janssens-Maenhout, G., Crippa, M., Guizzardi, D., Muntean, M., Schaaf, E., Dentener, F.,
729 Bergamaschi, P., Pagliari, V., Olivier, J. G. J., Peters, J. A. H. W., van Aardenne, J. A., Monni, S.,
730 Doering, U., Petrescu, A. M. R., Solazzo, E., and Oreggioni, G. D.: EDGAR v4.3.2 Global Atlas
731 of the three major greenhouse gas emissions for the period 1970–2012, *Earth Syst. Sci. Data*,
732 11, 959-1002, 10.5194/essd-11-959-2019, 2019.
733
734 Kuenen, J., Dellaert, S., Visschedijk, A., Jalkanen, J. P., Super, I., and Denier van der Gon, H.:
735 CAMS-REG-v4: a state-of-the-art high-resolution European emission inventory for air quality
736 modelling, *Earth Syst. Sci. Data*, 14, 491-515, 10.5194/essd-14-491-2022, 2022.
737
738 Kuttippurath, J., Patel, V. K., Kashyap, R., Singh, A., and Clerbaux, C.: Anomalous increase in
739 global atmospheric ammonia during COVID-19 lockdown: Need policies to curb agricultural
740 emissions, *Journal of Cleaner Production*, 434, 140424,
741 <https://doi.org/10.1016/j.jclepro.2023.140424>, 2024.
742
743 Li, C., Martin, R. V., Shephard, M. W., Cady-Pereira, K., Cooper, M. J., Kaiser, J., Lee, C. J.,
744 Zhang, L., and Henze, D. K.: Assessing the Iterative Finite Difference Mass Balance and 4D-
745 Var Methods to Derive Ammonia Emissions Over North America Using Synthetic
746 Observations, *Journal of Geophysical Research: Atmospheres*, 124, 4222-4236,
747 <https://doi.org/10.1029/2018JD030183>, 2019.
748

749 Liu, F., van der A, R. J., Eskes, H., Ding, J., and Mijling, B.: Evaluation of modeling NO₂
750 concentrations driven by satellite-derived and bottom-up emission inventories using in situ
751 measurements over China, *Atmos. Chem. Phys.*, 18, 4171-4186, 10.5194/acp-18-4171-2018,
752 2018.
753
754 Lolkema, D. E., Noordijk, H., Stolk, A. P., Hoogerbrugge, R., van Zanten, M. C., and van Pul, W.
755 A. J.: The Measuring Ammonia in Nature (MAN) network in the Netherlands, *Biogeosciences*,
756 12, 5133-5142, 10.5194/bg-12-5133-2015, 2015.
757
758 Luo, Z., Zhang, Y., Chen, W., Van Damme, M., Coheur, P. F., and Clarisse, L.: Estimating global
759 ammonia (NH₃) emissions based on IASI observations from 2008 to 2018, *Atmos. Chem.*
760 *Phys.*, 22, 10375-10388, 10.5194/acp-22-10375-2022, 2022.
761
762 Menut, L., Bessagnet, B., Briant, R., Cholakian, A., Couvidat, F., Mailler, S., Pennel, R., Siour,
763 G., Tuccella, P., Turquety, S., and Valari, M.: The CHIMERE v2020r1 online chemistry-
764 transport model, *Geosci. Model Dev.*, 14, 6781-6811, 10.5194/gmd-14-6781-2021, 2021.
765
766 Menut, L., Bessagnet, B., Khvorostyanov, D., Beekmann, M., Blond, N., Colette, A., Coll, I.,
767 Curci, G., Foret, G., Hodzic, A., Mailler, S., Meleux, F., Monge, J. L., Pison, I., Siour, G.,
768 Turquety, S., Valari, M., Vautard, R., and Vivanco, M. G.: CHIMERE 2013: a model for regional
769 atmospheric composition modelling, *Geosci. Model Dev.*, 6, 981-1028, 10.5194/gmd-6-981-
770 2013, 2013.
771
772 Mijling, B. and van der A, R. J.: Using daily satellite observations to estimate emissions of
773 short-lived air pollutants on a mesoscopic scale, *Journal of Geophysical Research:*
774 *Atmospheres*, 117, 10.1029/2012JD017817, 2012.
775
776 Mijling, B., van der A, R. J., and Zhang, Q.: Regional nitrogen oxides emission trends in East
777 Asia observed from space, *Atmos. Chem. Phys.*, 13, 12003-12012, 10.5194/acp-13-12003-
778 2013, 2013.
779
780 Noordijk, H., Braam, M., Rutledge-Jonker, S., Hoogerbrugge, R., Stolk, A. P., and van Pul, W.
781 A. J.: Performance of the MAN ammonia monitoring network in the Netherlands,
782 *Atmospheric Environment*, 228, 117400, <https://doi.org/10.1016/j.atmosenv.2020.117400>,
783 2020.
784
785 Pinterits, M., B. Ullrich, T. Bartmann and M. Gager: European Union emission inventory
786 report 1990-2019 under the UNECE Convention on Long-range Transboundary Air Pollution
787 (Air Convention), EEA Report No 5/2021, 2021NEC, Air pollution in Europe: 2023 reporting
788 status under the National Emission reduction Commitments Directive, 2023
789 ([https://www.eea.europa.eu/publications/national-emission-reduction-commitments-](https://www.eea.europa.eu/publications/national-emission-reduction-commitments-directive-2023/air-pollution-in-europe-2023)
790 [directive-2023/air-pollution-in-europe-2023](https://www.eea.europa.eu/publications/national-emission-reduction-commitments-directive-2023/air-pollution-in-europe-2023)), 2023.
791
792 Renard, J. J., Calidonna, S. E., and Henley, M. V.: Fate of ammonia in the atmosphere—a
793 review for applicability to hazardous releases, *Journal of Hazardous Materials*, 108, 29-60,
794 <https://doi.org/10.1016/j.jhazmat.2004.01.015>, 2004.
795

796 Rijdsdijk, P., Eskes, H., Dingemans, A., Boersma, F., Sekiya, T., Miyazaki, K., and Houweling, S.:
797 Quantifying uncertainties of satellite NO₂ superobservations for data assimilation and model
798 evaluation, *EGUsphere*, 2024, 1-42, 10.5194/egusphere-2024-632, 2024.
799

800 Schaap, M., van Loon, M., ten Brink, H. M., Dentener, F. J., and Builtjes, P. J. H.: Secondary
801 inorganic aerosol simulations for Europe with special attention to nitrate, *Atmos. Chem.*
802 *Phys.*, 4, 857-874, 10.5194/acp-4-857-2004, 2004.
803

804 Shephard, M. W. and Cady-Pereira, K. E.: Cross-track Infrared Sounder (CrIS) satellite
805 observations of tropospheric ammonia, *Atmos. Meas. Tech.*, 8, 1323-1336, 10.5194/amt-8-
806 1323-2015, 2015.
807

808 Shephard, M. W., Dammers, E., Cady-Pereira, K. E., Kharol, S. K., Thompson, J., Gainariu-
809 Matz, Y., Zhang, J., McLinden, C. A., Kovachik, A., Moran, M., Bittman, S., Sioris, C. E., Griffin,
810 D., Alvarado, M. J., Lonsdale, C., Savic-Jovicic, V., and Zheng, Q.: Ammonia measurements
811 from space with the Cross-track Infrared Sounder: characteristics and applications, *Atmos.*
812 *Chem. Phys.*, 20, 2277-2302, 10.5194/acp-20-2277-2020, 2020.
813

814 Sitwell, M., Shephard, M. W., Rochon, Y., Cady-Pereira, K., and Dammers, E.: An ensemble-
815 variational inversion system for the estimation of ammonia emissions using CrIS satellite
816 ammonia retrievals, *Atmos. Chem. Phys.*, 22, 6595-6624, 10.5194/acp-22-6595-2022, 2022.
817

818 Soulie, A., C. Granier, S. Darras, N. Zilbermann, T. Doumbia, M. Guevara, J.-P. Jalkanen, S.
819 Keita, C. Lioussé, M. Crippa, D. Guizzardi, R. Hoesly, and Smith, S. J.: Global Anthropogenic
820 Emissions (CAM5-GLOB-ANT) for the Copernicus Atmosphere Monitoring Service Simulations
821 of Air Quality Forecasts and Reanalyses, *Earth Syst. Sci. Data*, 2023.
822

823 Van Damme, M., Clarisse, L., Whitburn, S., Hadji-Lazaro, J., Hurtmans, D., Clerbaux, C., and
824 Coheur, P.-F.: Industrial and agricultural ammonia point sources exposed, *Nature*, 564, 99-
825 103, 10.1038/s41586-018-0747-1, 2018.
826

827 Van Damme, M., Clarisse, L., Franco, B., Sutton, M. A., Erisman, J. W., Wichink Kruit, R., van
828 Zanten, M., Whitburn, S., Hadji-Lazaro, J., Hurtmans, D., Clerbaux, C., and Coheur, P.-F.:
829 Global, regional and national trends of atmospheric ammonia derived from a decadal (2008–
830 2018) satellite record, *Environmental Research Letters*, 16, 055017, 10.1088/1748-
831 9326/abd5e0, 2021.
832

833 van der A, R. J., Ding, J., and Eskes, H.: Monitoring European anthropogenic NO_x emissions
834 from space, *Atmos. Chem. Phys.*, 24, 7523-7534, 10.5194/acp-24-7523-2024, 2024.
835

836 van der A, R. J., de Laat, A. T. J., Ding, J., and Eskes, H. J.: Connecting the dots: NO_x emissions
837 along a West Siberian natural gas pipeline, *npj Climate and Atmospheric Science*, 3, 16,
838 10.1038/s41612-020-0119-z, 2020.
839

840 van der A, R. J., Mijling, B., Ding, J., Koukouli, M. E., Liu, F., Li, Q., Mao, H., and Theys, N.:
841 Cleaning up the air: effectiveness of air quality policy for SO₂ and NO_x emissions in China,
842 *Atmos. Chem. Phys.*, 17, 1775-1789, 10.5194/acp-17-1775-2017, 2017.

843
844 van der Graaf, S., Dammers, E., Segers, A., Kranenburg, R., Schaap, M., Shephard, M. W., and
845 Erisman, J. W.: Data assimilation of CrIS NH₃ satellite observations for improving
846 spatiotemporal NH₃ distributions in LOTOS-EUROS, *Atmos. Chem. Phys.*, 22, 951-972,
847 10.5194/acp-22-951-2022, 2022.
848
849 van Geffen, J. H. G. M., Eskes, H. J., Boersma, K. F., and Veefkind, J. P.: TROPOMI ATBD of the
850 total and tropospheric NO₂ data products, Report S5P-KNMI-L2-0005-RP, version 2.4.0,
851 202207-11, KNMI, De Bilt, The Netherlands,,
852 [https://sentinel.esa.int/documents/247904/2476257/Sentinel-5P-TROPOMI-ATBD-NO2-](https://sentinel.esa.int/documents/247904/2476257/Sentinel-5P-TROPOMI-ATBD-NO2-data-products)
853 [data-products](https://sentinel.esa.int/documents/247904/2476257/Sentinel-5P-TROPOMI-ATBD-NO2-data-products) (last access: 23 Nov. 2023), 2022.
854
855 Veefkind, J. P., Aben, I., McMullan, K., Förster, H., de Vries, J., Otter, G., Claas, J., Eskes, H. J.,
856 de Haan, J. F., Kleipool, Q., van Weele, M., Hasekamp, O., Hoogeveen, R., Landgraf, J., Snel,
857 R., Tol, P., Ingmann, P., Voors, R., Kruizinga, B., Vink, R., Visser, H., and Levelt, P. F.: TROPOMI
858 on the ESA Sentinel-5 Precursor: A GMES mission for global observations of the atmospheric
859 composition for climate, air quality and ozone layer applications, *Remote Sensing of*
860 *Environment*, 120, 70-83, <http://dx.doi.org/10.1016/j.rse.2011.09.027>, 2012.
861
862 White, E., Shephard, M. W., Cady-Pereira, K. E., Kharol, S. K., Ford, S., Dammers, E., Chow, E.,
863 Thiessen, N., Tobin, D., Quinn, G., O'Brien, J., and Bash, J.: Accounting for Non-Detects:
864 Application to Satellite Ammonia Observations, *Remote Sensing*, 15, 2610, 2023.
865
866 Wyer, K. E., Kelleghan, D. B., Blanes-Vidal, V., Schauburger, G., and Curran, T. P.: Ammonia
867 emissions from agriculture and their contribution to fine particulate matter: A review of
868 implications for human health, *Journal of Environmental Management*, 323, 116285,
869 <https://doi.org/10.1016/j.jenvman.2022.116285>, 2022.
870
871 Zavyalov, V., Esplin, M., Scott, D., Esplin, B., Bingham, G., Hoffman, E., Lietzke, C., Predina, J.,
872 Frain, R., Suwinski, L., Han, Y., Major, C., Graham, B., and Phillips, L.: Noise performance of
873 the CrIS instrument, *Journal of Geophysical Research: Atmospheres*, 118, 13,108-113,120,
874 <https://doi.org/10.1002/2013JD020457>, 2013.
875
876 Zhang, L., Chen, Y., Zhao, Y., Henze, D. K., Zhu, L., Song, Y., Paulot, F., Liu, X., Pan, Y., Lin, Y.,
877 and Huang, B.: Agricultural ammonia emissions in China: reconciling bottom-up and top-
878 down estimates, *Atmos. Chem. Phys.*, 18, 339-355, 10.5194/acp-18-339-2018, 2018.
879
880 Zhang, X., Gu, B., van Grinsven, H., Lam, S. K., Liang, X., Bai, M., and Chen, D.: Societal
881 benefits of halving agricultural ammonia emissions in China far exceed the abatement costs,
882 *Nature Communications*, 11, 4357, 10.1038/s41467-020-18196-z, 2020.
883
884 Zhu, L., Henze, D. K., Cady-Pereira, K. E., Shephard, M. W., Luo, M., Pinder, R. W., Bash, J. O.,
885 and Jeong, G.-R.: Constraining U.S. ammonia emissions using TES remote sensing
886 observations and the GEOS-Chem adjoint model, *Journal of Geophysical Research:*
887 *Atmospheres*, 118, 3355-3368, <https://doi.org/10.1002/jgrd.50166>, 2013.
888
889

